THE ASTROPHYSICAL JOURNAL, 410:796–802, 1993 June 20

RESOLVING THE IRON K LINE IN CYGNUS X-2: AN OBSERVATION WITH BBXRT

A. P. SMALE,[1] C. DONE, R. F. MUSHOTZKY, K. A. WEAVER,[2] P. J. SERLEMITSOS, F. E. MARSHALL, R. PETRE, K. M. JAHODA, E. A. BOLDT, J. H. SWANK, A. E. SZYMKOWIAK, R. L. KELLEY, AND K. ARNAUD[2]
Laboratory for High-Energy Astrophysics, Code 666, NASA/Goddard Space Flight Center, Greenbelt, MD 20771
Received 1992 September 30; accepted 1992 December 18

ABSTRACT

We present the first high-quality, moderate-resolution spectroscopy of Cygnus X-2 in the 0.4–12 keV energy range, obtained using the Broad Band X-Ray Telescope (BBXRT), part of the *Astro-1* shuttle payload. These data enable us to resolve the physical width of the 6.7 keV Fe Kα feature in Cyg X-2 with an energy resolution a factor of 4 better than previous X-ray experiments. The feature is modeled well with a single broad Gaussian line with center energy $E = 6.71(+0.23; -0.20)$, full width half-maximum $971(+505; -376)$ eV, and equivalent width 60 ± 27 eV. There is also tentative evidence for Fe L line emission at 1 keV. A sensitive search for an iron edge feature in the 7–9 keV range results in an upper limit on the absorption depth of $\tau \leq 0.15$.

There are three possible sites for the Fe Kα emission: the accretion disk, its corona, or the source itself. The last can be rejected as the continuum spectrum suggests that the central $kT \sim 1.7$ keV blackbody is Comptonized through $\tau \sim 20$. Any line would thus be strongly downscattered, broadened, and lost. An origin in a corona covering the source and disk can also be ruled out as the observed broad line can be produced only in material with $\tau \sim 3$, far in excess of the limits on the optical depth at the iron edge. A line from an optically thick corona out of the line of sight would be viewed only by reflection rather than transmission, so the photons would travel through $\tau \sim 1$, also inconsistent with the lack of an iron edge. Reflection from the accretion disk itself, however, can produce a line of the observed energy, width, and equivalent width if the disk surface is highly ionized.

Subject headings: binaries: close — stars: individual (Cygnus X-2) — X-rays: stars

1. INTRODUCTION

The low-mass X-ray binary (LMXB) Cygnus X-2 consists of a 1.4 $M_\odot$ neutron star and an evolved, late-type $\sim 0.7\ M_\odot$ companion (Cowley, Crampton, & Hutchings 1979, hereafter CCH; McClintock et al. 1984). The apparent spectral type of V1341 Cyg, its optical counterpart, varies from A5 to F2 around the 9.84 day binary cycle, probably due to X-ray reprocessing in the heated face of the companion, and the radial velocity variations imply a system inclination of $\sim 70°$ (CCH). The compact object was unambiguously identified as a neutron star after a weak X-ray burst was observed from the system (Kahn & Grindlay 1984). Assuming the system is powered by Roche lobe overflow, Cyg X-2 is 8 kpc distant.

At X-ray energies, Cyg X-2 displays a variety of temporal and spectral phenomena. In its high state it shows irregular short-term (~minute to ~hr) dips with depths up to 60% of the nondip flux. These dips divide into three categories, defined by the differing luminosity/hardness variations they exhibit (Vrtilek et al. 1988). The phase-dependent absorption dips are probably caused by clumps of accreting material passing through the line of sight at a radius of $\sim 3\ R_\odot$; this interpretation is supported by the detection of an absorption feature at 14 Å during such dips (Vrtilek et al. 1986). At lower intensity states (L_x [2–10 keV] $< 7 \times 10^{37}$ ergs s^{-1}) this dipping activity is not seen, and a modulation of the X-ray flux is observed, with a 3 day decrease in intensity at binary phase 0.4–0.8, perhaps corresponding to the obscuration of an accretion disk corona (ADC) by a tilted accretion disk (Vrtilek et al. 1988). In the high state the disk becomes geometrically thick but optically thin, and this obscuration of the ADC does not occur.

Like several other bright binaries, Cyg X-2 follows a Z-shaped correlation curve on an X-ray color-color diagram (e.g., Schulz, Hasinger, & Trümper 1989). The source moves along this Z-curve on a time scale of hours, never jumping discontinuously from state to state. On the horizontal (top) branch of the color-color diagram the power spectrum of the source reveals quasi-periodic oscillations with a frequency of 18–55 Hz, along with lower frequency noise. On the normal branch (the central portion of the Z), Quasi-periodic oscillations (QPOs) with a frequency of ~5 Hz are observed. This frequency increases steadily to 10–20 Hz as the source goes into the flaring branch (Hasinger et al. 1990; see also Stella 1988; van der Klis 1989 for reviews of QPO behavior). From extended *Ginga* observations of Cyg X-2, Hasinger et al. (1990) showed that the source stayed on the horizontal branch for 0.5–1 day, and the normal and flaring branches for 0.2–0.4 day, completing a full passage along the Z-curve in 2 days.

The study of iron emission lines in LMXBs took a major step forward wth the launch of gas scintillation proportional counters (GSPCs) on *Tenma* and *EXOSAT*. These instruments had an energy resolution of ~10% at 6 keV, better than the proportional counters previously flown by a factor of ~2, and this improvement enabled investigators to resolve the broad iron K line in Sco X-1 (White, Peacock, & Taylor 1985) and detect similar features in several other bright sources (e.g., White et al. 1986; Hirano et al. 1987). Emission at the 6.7 keV line is now known to be a common feature in LMXBs; the line is identified with the Kα radiative transitions of helium-like

[1] Also Research Scientist, Universities Space Research Association.
[2] Also University of Maryland.

iron, probably caused by recombination in the inner disk or coronal regions.

The solid-state detectors in the current generation of space-borne instruments provide a similar enhancement of our ability to study line emission in LMXBs; the intrinsic energy resolution of the BBXRT detectors flown in 1990 December represents a factor of ~ 4 improvement over the GSPCs at 6 keV. BBXRT observed several LMXBs during its 9 day mission; here we present an analysis of the spectrum of Cygnus X-2. In § 2 we describe the BBXRT experiment, the Cyg X-2 observations, and calibration details, and in § 3 we present the spectral fitting results. In § 4 we put the BBXRT observation into the broader context by comparisons with other data sets in the literature and discuss the physical significance of our findings. The detailed analysis we have been able to perform even from the comparatively short observation possible with BBXRT provides a good illustration of the power and sensitivity of solid-state detectors in the study of line and edge features in LMXBs.

2. THE BBXRT OBSERVATIONS

The Broad-Band X-Ray Telescope (BBXRT) was flown on the space shuttle *Columbia* (STS-35) on 1990 December 2–11, as part of the *Astro-1* payload. The flight of BBXRT marked the first opportunity for performing X-ray observations over a broad energy range (0.3–12 keV) with a moderate energy resolution (typically 90 eV and 150 eV at 1 and 6 keV, respectively). This energy resolution coupled with an extremely low detector background of 1.2×10^{-3} counts keV^{-1} s^{-1} makes BBXRT a very powerful tool for the study of continuum and line emission from X-ray binaries and other cosmic sources.

The BBXRT instrument (Serlemitsos et al. 1992) consists of two co-aligned telescopes of 3.8 m focal length. Each telescope contains a thin-foil conical mirror assembly consisting of 118 curved, gold-plated aluminum reflectors, and a segmented, cryogenically cooled Si(Li) detector at the focal plane. Each of the detectors, A and B, is subdivided into five pixels each with 512 energy channels. The central pixels (A0, B0) have a field of view 4′ in diameter, and the outer pixels (A1–A4, B1–B4) extend the total field of view to a diameter of 17.′4. The B detectors are rotated relative by 180° relative to the A detectors such that, e.g., A1 and B3 co-observe the same area on the sky.

Cygnus X-2 was observed twice during the mission; on 1990 December 6 06:11 UT for 864 s, and on December 6 19:52 UT for 660 s. These times correspond to phases $\phi \sim 0.00$ and $\phi \sim 0.06$ in the 9.84 day orbital cycle using the ephemeris of Crampton & Cowley (1980). (Note that the ephemeris of Cyg X-2 was originally derived using optical spectroscopy, thus the neutron star is in front of the F star companion at $\phi = 0$ and X-ray minimum occurs at $\phi \sim 0.6$.) During the first observation, the source was well centered on the detectors and produced a total count rate in all pixels of 964 counts s^{-1}. Using ray tracing we find an off-axis angle of 0.′90 in A and 1.′32 in B (there is a known small misalignment between the A and B telescopes).

Preflight calibration of the mirror point-spread function showed that for a point source aligned in the central pixel, 62% of the events are detected by the central detector, with 17% spread between the four outer pixels and 21% being vignetted by the interpixel mask. Our in-flight results bear this out, with count rates in the A0 and B0 pixels of 378.8 counts s^{-1} and 284.9 counts s^{-1} respectively, making up 72% and 65% of the total A and B count rates. For the first observation we will concentrate on the data from the central pixels, noting that the outer pixels give consistent spectral parameters.

For the second observation the ray tracing calculation is confirmed by a precise pointing position measured using the onboard aspect camera. The off-axis angle was 2.′55 in A and 1.′75 in B, and most of the counts fell in the A3, A4, B0, and B1 pixels (21% and 46% of the counts fell in the central A0 and B0 elements).

Both observations were performed during orbit day, with a Sun angle of 90° and an Earth angle of $\sim 120°$. For fainter BBXRT targets, soft X-ray emission from the illuminated atmosphere of the Earth is evident in the raw data below 0.7 keV. In the slew interval immediately preceding the Cyg X-2 observation this bright Earth emission has an amplitude of $\lesssim 0.2$ counts s^{-1}.

For a source as bright as Cyg X-2 this effect is clearly negligible. The brightness of Cyg X-2 also makes the subtraction of detector background superfluous; several background subtraction schemes were attempted and none affected the results of spectral fitting by more than 1%. Neither of the observations suffered from contamination by the South Atlantic Anomaly.

The BBXRT detector response matrices have been painstakingly constructed based on data from prelaunch, in-flight, and postflight calibrations. Before launch, measurements of the effective area of the mirrors and the detector efficiencies were performed at GSFC. During the mission the Crab Nebula was observed on several occasions, and frequent calibrations obtained using an internal Fe^{55} source. More detailed modeling of partial charge in the detectors, and adjustments for the gold M edge in the mirrors and Al and Si edges in the detectors, have been performed since the flight of BBXRT, using further ground calibration data obtained at GSFC and the National Institute for Standards and Technology in 1991 and 1992. The systematic residuals from a power law fit to data from the Crab Nebula show no features larger than 5% between 0.5 and 8 keV and 10% between 8 and 12 keV, and no narrow features in the spectrum with an equivalent width greater than 12 eV. A 10% residual uncertainty still persists at ~ 0.4–0.5 keV. A full description of the BBXRT calibration process can be found in Weaver et al. (1992).

3. RESULTS

Examining the light curves for our observations of Cygnus X-2 we find no evidence for dipping or flaring activity. There are no flux variations greater than 5%, and no significant variations in hardness during either observation.

In Figure 1 we show the BBXRT spectra from the central pixels (A0, B0) for the first observation of Cygnus X-2. Table 1 contains the parameters and χ^2 values obtained from simultaneous fits to both spectra, using a variety of single-component and two-component models. Included in these fits were two narrow Gaussian features with fixed parameters; an absorption feature at 1.57 keV and an emission feature at 2.21 keV, each with an equivalent width of 9 eV. These features remove the contributions to χ^2 from known small inaccuracies in the theoretical models of the Al K and gold M edges. After the Crab Nebula, Cygnus X-2 was the brightest source observed with BBXRT, and the signal-to-noise ratio of the data is so high that these very small effects need to be compensated for.

The best fit to the continuum emission from Cygnus X-2 was found to be a two-component model consisting of a Comptonization spectrum (Sunyaev & Titarchuk 1980) plus a 0.63

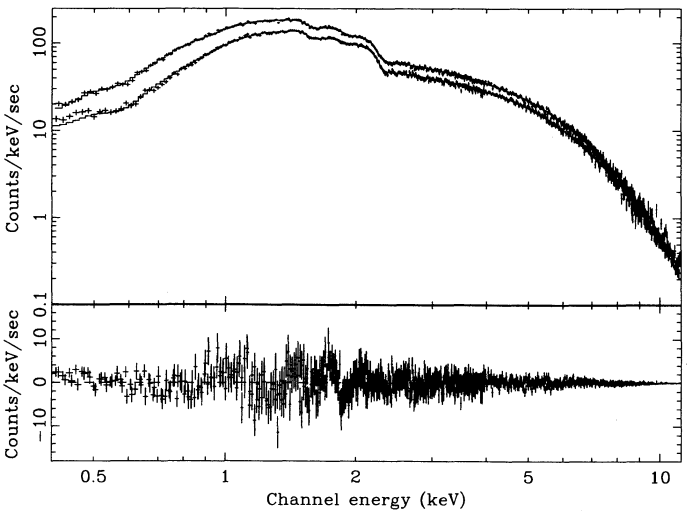

FIG. 1.—The spectra and best fit for the first BBXRT observation of Cygnus X-2 on 1990 December 6 06:11 UT. The top panel shows the accumulated spectra from the two central pixels, fit using a two-component Sunyaev & Titarchuk Comptonization continuum plus a 0.63 keV blackbody as described in the text. The lower panel shows the residuals to this fit; with the exception of a possible excess at ~1 keV, other features have instrumental origins.

keV blackbody. This model combination has been generally successful in modeling spectra of X-ray binary accretion disks (White, Stella, & Parmar 1988) and has a plausible physical interpretation, with the Comptonization component arising from the upscattering of cool photons on hot electrons in the accretion disk and the blackbody component traditionally being associated with the optically thick boundary layer between the accretion disk and the surface of the neutron star. The derived optical depth of $\tau = 21$ leads to a Comptonization y-parameter of ~5, and the temperature is $kT = 1.70 \pm 0.04$ keV. The total luminosity of Cyg X-2 in the 1–10 keV band was $L_x \sim 0.9$–1.2×10^{38} ergs s^{-1}, assuming a distance of 8 kpc, placing it in the "high" luminosity state, and the blackbody component makes up ~10% of this flux.

Even with the inclusion of the instrumental features, the χ^2 for the best fit was 1045 for 960 dof, still not formally acceptable. Looking more closely at the 5–8 keV region, a broad excess of counts is clearly visible in the residuals (Fig. 2*a*) at 6.7 keV. Note that this figure contains the *true* residuals to the continuum fit, and is *not* the result of fitting a line and then setting the normalization of the line to zero to maximize its apparent size for presentation purposes, a rather misleading practice often encountered in the literature. Presenting this information in a different way, we also show the data divided by the model, binned appropriately, in Figure 2*b*. To illustrate

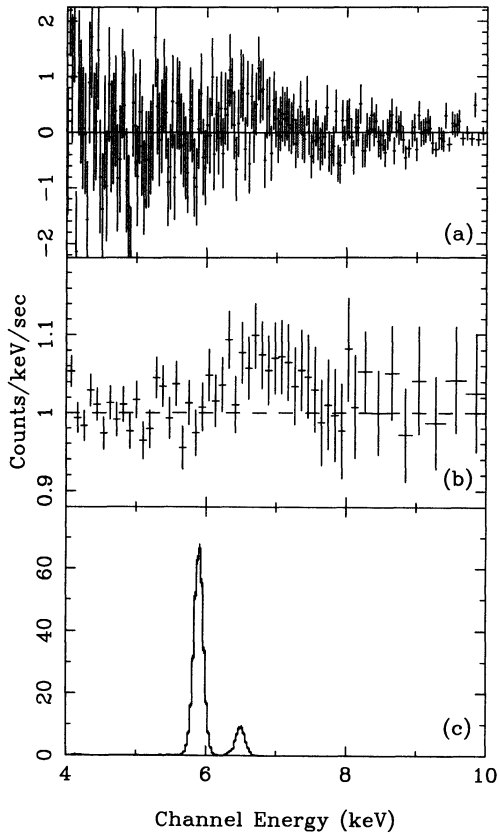

FIG. 2.—(*a*) A close-up of the residuals to a two-component continuum fit to the data around the 6.7 keV region, for the first observation of Cyg X-2. Note that this figure was *not* created by fitting a line and then setting its normalization to zero, but shows the *true* residual. (*b*) The data divided by the model for the same energy region, binned to maximize the signal-to-noise ratio. (*c*) On the same scale, an in-flight Fe^{55} calibration run performed 8 hr prior to the first observation, as a graphic illustration of the energy resolution of BBXRT around the region of interest.

the resolution of BBXRT in the 6 keV region, Figure 2*c* contains the spectrum of an in-flight iron calibration run performed 8 hr before the first observation of Cygnus X-2.

Including a single broad Gaussian line in the spectral model we find that the feature has a center energy of $E = 6.71(+0.23; -0.20)$, consistent with iron K emission. A full width half-maximum (FWHM) of 971(+505; −376) eV, and an equivalent width (EW) of 60 ± 27 eV. This is the first direct measurement of the physical width of the iron line in Cygnus X-2 that we can find quoted in the literature; in analyses of previous data sets the width of the line was fixed at

TABLE 1

CONTINUUM SPECTRAL FITS TO THE BBXRT DATA FROM CYGNUS X-2

Model	Column	Parameter	Parameter	Normalization	χ^2/dof
Power law	4.35×10^{21} cm^{-2}	$\alpha = 1.899$	...	$N = 4.021$	9055/972
Thermal bremstrahlung	3.10×10^{21}	$kT = 6.99$ keV	...	$N = 1.498$	2878/972
Blackbody	0	$kT = 0.875$ keV	...	$N = 0.160$	27195/972
Power law + cutoff	$(2.09 \pm 0.04) \times 10^{21}$	$\alpha = 0.718 \pm 0.023$	$E_{cut} = 3.32 \pm 0.06$ keV	$N = 3.021$	1105/971
Compt. S&T	$(3.12 \pm 0.04) \times 10^{21}$	$kT = 1.61 \pm 0.01$ keV	$\tau = 20.4 \pm 0.2$	$N = 2.937$	1292/971
Thermal bremsstrahlung	$(2.70 \pm 0.04) \times 10^{21}$	$kT_1 = 5.61 \pm 0.22$ keV	...	$N_1 = 1.3915$	1127/961
+ blackbody		$kT_2 = 1.21 \pm 0.03$ keV	...	$N_2 = 0.0442$	
Compt. S&T	$(2.61 \pm 0.08) \times 10^{21}$	$kT_1 = 1.70 \pm 0.04$ keV	$\tau = 21.0 \pm 0.6$	$N_1 = 2.337$	1045/960
+ blackbody		$kT_2 = 0.627 \pm 0.037$ keV	...	$N_2 = 0.0226$	

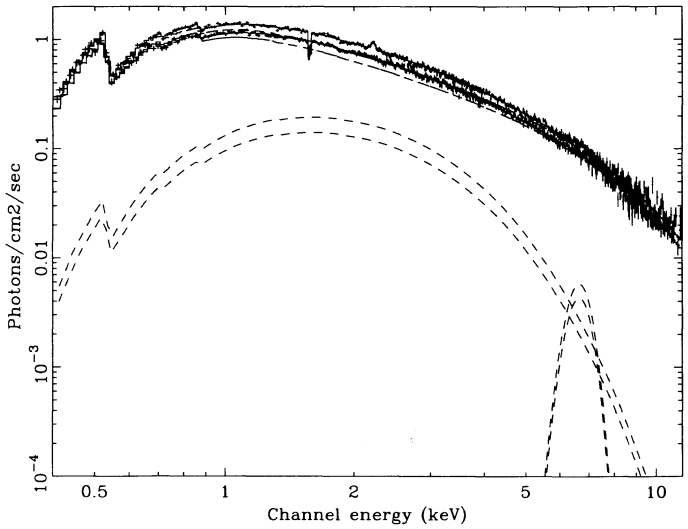

FIG. 3.—The unfolded spectrum of Cygnus X-2, with the individual components of the fit plotted with dashed lines. The small features at 2.2 keV and 1.6 keV are associated with residual instrumental effects.

1 keV, which we can now see was a good approximation. Examination of residuals to this single-Gaussian fit show no indication of structure within the iron K emission. In Figure 3 we show the unfolded spectrum of Cygnus X-2, and in Figure 4, the confidence contours for the physical width and center energy of the 6.7 keV line, derived from a two-dimensional χ^2 grid.

A single Gaussian is not a unique fit to the broad feature, although it has the smallest number of free parameters. The feature can also be well fitted with a combination of two Gaussians, the first at 6.9 keV with FWHM = 880 eV, EW = 50 eV and the second at 6.3 keV with FWHM = 500 eV, EW = 15 eV. All the parameters were allowed to be free in the fit, but the improvement in χ^2 from the addition of the second Gaussian component was not statistically significant. Another combination of two Gaussians, consisting of a broad line with all parameters allowed to be free, and a line forced to be narrow, resulted in a 3 σ upper limit of 10 eV for the equivalent width of the narrow component.

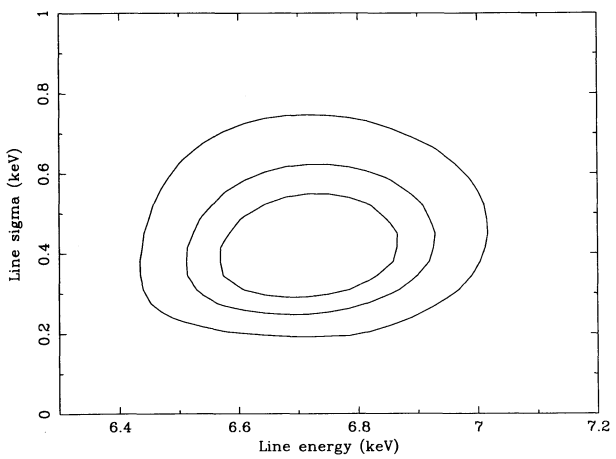

FIG. 4.—The χ^2 contours for the fitted values of the line energy and the line σ in keV (FWHM = 2.354 σ), derived from a two-dimensional grid. The contours represent changes in χ^2 of 2.30, 4.61, and 9.21, as appropriate for 1 σ, 90%, and 99% for two parameters of interest.

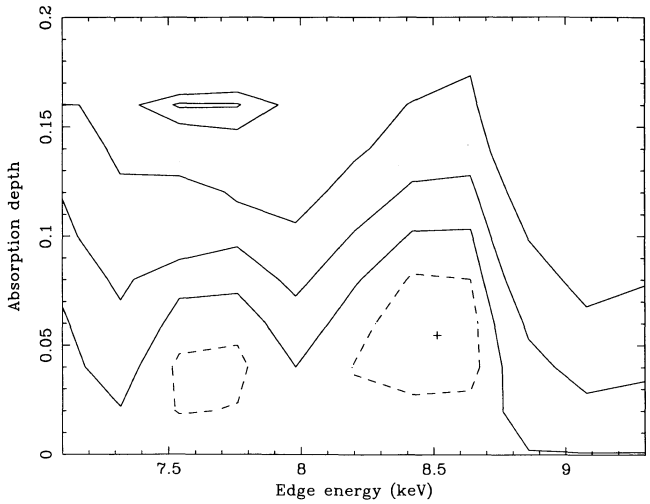

FIG. 5.—Confidence contours for the values of edge energy and absorption depth from a two-dimensional gridding of the data. In both cases the solid-line contours represent χ^2 changes of 2.30, 4.61, and 9.21. The dotted line denotes a χ^2 change of 1.0. The χ^2 minimum from which the contours are measured is marked with a small cross.

An additional low-level feature is visible in the residual plot in Figure 1 at $\sim$1 keV. The inclusion of a Gaussian at an energy of 0.99 $\pm$ 0.04 keV, with a FWHM between 50 and 235 eV and an equivalent width of 8 eV, reduces χ^2 by 22. This feature is not seen in the residuals for BBXRT observations of the Crab (Weaver et al. 1992), and we tentatively associate it with iron L emission. However, this feature has a magnitude close to the accuracy with which the BBXRT response matrices are currently known, and similar in size to the remaining fluctuations at $\sim$1.6 and 1.8 keV due to the Al and Si edges, and we therefore consider this identification to be preliminary.

The good energy resolution and high S/N ratio of the BBXRT data make it the most sensitive data set yet to search for the presence of an iron edge. We have constructed a two-dimensional χ^2 grid by stepping the energy and absorption depth through a range of values and for each combination finding the χ^2 minimum, with all other parameters allowed to be free. Examining this grid over the energy range 7–9 keV, we find the 99% upper limit on the absorption depth of an edge feature to be $\tau < 0.15$. Figure 5 shows the confidence contours for this search.

Fitting the spectra accumulated in the relevant pixels (A3, A4, B0, B1) for the second observation, we obtain similar results for the Comptonization component, with a slightly lower temperature of $kT = 1.39 \pm 0.02$, and $\tau = 21.1 \pm 0.3$. For these data, the blackbody component is less well defined due to the lower count rate and is not, in fact, required by the statistics. The iron line is still detected but, again due to the lower count rate, we do not resolve its physical width. Fixing the width of the iron line at FWHM = 1 keV, we obtain a line energy of 6.7 $\pm$ 0.2 keV and an equivalent width of 72 $\pm$ 30 eV.

4. DISCUSSION

4.1. *The BBXRT Results in the Context of Previous Observations*

The exposure time and phase coverage of the BBXRT data are small compared to the typical duration of observations performed with, e.g., the *Einstein* and *EXOSAT* satellites.

While the BBXRT data have a higher spectral resolution, the satellite data have greater possibilities for temporal studies. Thus, it is important to put the BBXRT results in a broader context by comparing them with previous data sets.

Where the continuum spectral emission is concerned, there is no discrepancy between the BBXRT results and previous observations. Hasinger et al. (1990) show that for their extensive *Ginga* data set, the spectra in all three branches of the Z-diagram can be well fitted using a combination of an unsaturated Comptonized component and a blackbody component, with parameters similar to those we derive from BBXRT data. They note that this model predicts that the mass accretion rate $\dot{M}$ should increase as the source goes from the horizontal branch, through the normal branch to the flaring branch, consistent with current models for the QPO behavior, and is thus preferable to the model proposed by Mitsuda et al. (1984, 1989) consisting of a multitemperature disk blackbody plus simple blackbody, which predicts the reverse correlation. In their analysis of *EXOSAT* data, Chiappetti et al. (1990) favored a two-component thermal bremsstrahlung plus blackbody model, following on from the single-component thermal bremsstrahlung fits to *Einstein* MPC data of Vrtilek et al. (1986). However, this parameterization suffers from the difficulty that the luminosity of Cyg X-2 would require an emission measure four orders of magnitude higher than the available volume of the combined neutron star surface, accretion disk, and environs, as originally noted by Hirano et al. (1984). In addition, we have reexamined the *EXOSAT* data from Cygnus X-2, performing two-component fits to each spectrum in the HEASARC data base and find that in each case a Comptonization plus blackbody parameterization fits the ME+GSPC data as well as, and sometimes much better than, a bremsstrahlung plus blackbody model. From Table 1 we can see that for the BBXRT data the Comptonization plus blackbody model is preferred on statistical grounds. The evidence in favor of the Comptonization model is compelling.

While our BBXRT observations were clearly too short to enable us to directly determine which behavioral branch Cyg X-2 occupied on the Z-diagram, we can combine the spectral parameters we derive with the instrumental responses of previous missions to infer this indirectly. Our justification for attempting this stems from experiments that suggest that despite the overall long-term variability in the flux from Cyg X-2, the flux changes are not accompanied by large variations in the spectral form; therefore the color-color diagrams of different observations are not dissimilar. In fact, the results of this exercise have a pleasing consistency, confirming that the overall spectral behavior of Cyg X-2 is reliable on a time scale of years.

First, we folded our incident spectrum through the response matrix of the *Ginga* LAC. From the output of this convolution, we derived the expected values for the hardness and softness ratios used by Hasinger et al. (1990), and examined their hardness/intensity and color/color diagrams (Figs. 2 and 3, Hasinger et al. 1990) to see where our data points fell on these diagrams. The BBXRT data points lie in the lower third of the normal branch.

Next, we folded our spectrum through the response of the *EXOSAT* Medium Energy detectors, constructing the appropriate hardness and softness ratios and comparing them to the color/color plots in Schulz et al. (1989). This led to the same conclusion; that the source was occupying the lower normal branch at the time of the BBXRT observations. Finally, a fold through the *Einstein* MPC response led to a hardness/intensity relation consistent with a position in section E of the correlation plot in Vrtilek et al. (1986). Section E data were obtained between the Cyg X-2 orbital phases of 0.95 and 0.05, adding to our confidence in the internal consistency of the data sets and the behavior of the source over many years.

To summarize: during the BBXRT observations, the source was in a high state, on the lower portion of the normal branch of the color/color Z-diagram.

4.2. *Continuum and Line Emission from Cyg X-2*

The parameters we measure for the emission line in Cyg X-2 with BBXRT are not in serious disagreement with previous determinations. Using *Tenma* Hirano et al. (1987) found a significant 30 eV line with a FWHM of $\lesssim 740$ eV in one out of four observations. Using the *EXOSAT* GSPC, Chiappetti et al. significantly detected the iron line in two out of five observations (one at $\phi = 0.0$, the same phase as our BBXRT observation), with an equivalent width of ~ 60 eV, but did not quote a physical width. These general characteristics are also similar to those observed from other sources; Sco X-1 has a 6.75 keV line with an equivalent width of 25–50 eV and a FWHM of 0.7 keV (White et al. 1985), and the model fitting of several other sources suggests consistency with physical widths ~ 1 keV (e.g., White et al. 1986; Hirano et al. 1987).

We find a feature in our residuals at 1 keV, which is fitted well with a Gaussian with an equivalent width of 8 eV. Soft X-ray emission lines have been detected previously in the range 0.6–1.1 keV using the *Einstein* OGS (Vrtilek et al. 1986, 1991). While the source is on the flaring branch, O VIII Lyman α and β lines are observed. When the source moves onto the normal branch, the oxygen features are not seen, although emission at ~ 0.8 keV persists which may be associated with Fe XVII. The appearance of this complex of lines is very sensitive to the temperature of the emitting material (Kallman, Vrtilek, & Kahn 1989) and probably varies as a function of phase, mass transfer rate, and other variables. Further refinements in our low-energy calibration and in our ability to combine data from several BBXRT pixels will improve our sensitivity to low-energy features, and we will therefore return to the issue of the soft X-ray emission in a future paper.

The complex variability exhibited by Cyg X-2 suggests that dramatic changes in the appearance and structure of the accretion disk and corona take place on time scales shorter than a day. Based on the differing temporal and spectral behaviors in the high and low state, Vrtilek et al. (1988) describe a qualitative model for the system incorporating emission from the neutron star surface, a tilted, slaved accretion disk, and the accretion disk corona. In this model, the ADC is obscured by the disk between phases 0.4 and 0.8 during the low state. Accretion is relatively stable, and the X-ray light curve shows an orbital modulation correlated with the optical light curve. The transition into a high state leads to instability in the accretion process, and the disk is transformed from being geometrically thin and optically thick to geometrically thick and optically thin.

The presence of a magnetosphere in the system provides further complications to this picture. LMXBs with evolved companions such as Cyg X-2 should contain strong magnetic fields ($\sim 10^{10}$ G), requiring that the inner accretion disk terminates at the magnetosphere, some 150 km from the neutron star itself. The discovery of QPO from Cyg X-2 (Hasinger et al. 1986) supports this view. Hasinger et al. (1990) consider a

model where a geometrically thin accretion disk intersects a small magnetosphere at low accretion rates, in the horizontal branch. Turbulence at this intersection causes clumpiness of accreted material.

As the accretion rate increases, the inner disk puffs up to engulf the magnetosphere and the system moves onto the normal branch. As the accretion rate rises above the Eddington limit, the inner disk torus becomes still more distended and matter is ejected from the system now in the flaring branch of the Z-diagram.

This picture forms the basis for an understanding of the continuum and line emission observed using BBXRT. The system is on the normal branch, and thus the neutron star is effectively embedded in a dense cloud. The accretion disk is less extensive than it would be in the absence of a magnetosphere, and thus directly contributes only a small fraction of the X-ray emission. We postulate that the inner disk is responsible for the soft blackbody radiation we observe with $kT \sim 0.6$ keV. The emission from the surface of the neutron star and the boundary layer, also originally blackbody in form, is Comptonized in the dense cloud around the magnetosphere. Spectral fitting gives an original blackbody temperature of 1.7 keV, modified by a large number of scatterings in a plasma with $\tau \sim 20$. As the line photons scatter $\sim\tau^2$ times before escaping, any iron line produced by this Comptonizing plasma will be broadened and lost. Assuming that the Compton temperature of the radiation field is close to the blackbody temperature (10^7 K), then the line will be unrecognizable, with an energy of $\sim$1.6 keV and a physical width of $\sim$0.6 keV (Kallman & White 1989; Podznakov, Sobol, & Sunyaev 1983).

As the Comptonizing plasma cannot produce the observed line, the only other possible origins are the accretion disk itself or an ADC. As the line energy indicates ionized material, we first examine the possibility that the line is formed in the ADC (Kallman & White 1989). However, unless the corona is rotating with the disk, perhaps being towed by magnetic fields, then Comptonization is the only way to obtain line widths as large as 0.9 keV (as noted by White et al. 1986). This requires that $\tau \geq 3$ (Kallman & White 1989), corresponding to an optical depth at the iron edge of $\sim$3 for solar abundances. This is strongly ruled out by the BBXRT data, as the 99% confidence limit on the optical depth of the edge for any ionization state of iron is $\tau = 0.15$. To suppress the iron edge to this extent requires that only 5% of iron is at Fe XXVI, with the rest being completely stripped. The corona will then be at the Compton temperature of $\sim 10^7$ K, and the line will be downscattered to $\sim$6.1 keV and have a very low equivalent width (Kallman & White 1989; Kallman 1991).

Thus, the corona cannot be in the line of sight, leading us to consider a case where the ADC has a small scale height such that it overlies the accretion disk but does not extend over the central object. The limits on the optical depth are then no longer a constraint, so the corona can have $\tau \sim 3$. However, this geometry requires that the line is formed by reflection (rather than transmission) as the ADC is optically thick and illuminated by the central source. Reflection takes place at the $\tau \sim 1$ surface, with very little line produced at a depth of $\tau \sim 3$, so then the line width cannot be produced from Compton scattering.

The only other line broadening mechanism is Doppler motion from the rotation of the disk. For a flat disk of solar abundance inclined at 70°, illuminated by power-law emission with photon index 1.7 from a central optically thick source occupying the inner 5 R_s, a line with an equivalent width of $\sim$55 eV is predicted (Matt, Perola, & Piro 1991). However, the Comptonized spectrum has many fewer photons than a power law past the iron edge, and so will produce less line emission. While the lower energy part of the Compton spectrum resembles a power law of index 1.5, it has 58% fewer photons between 7.1 and 10 keV. This difference in the spectrum reduces the estimated equivalent width to $\sim$30 eV for a line caused by reflection from a Comptonized spectrum (George & Fabian 1991). This is only half of the observed value.

The physical width and centroid of the reflected line are predicted to be $\sigma = (\mathrm{FWHM}/2.35) \sim 0.8$ keV and E = 6.45 keV, respectively (Matt et al. 1992), too broad and too low in energy. However, as seen above, the optically thick illuminating source in Cyg X-2 is thought to extend out to radii of $\sim$150 km, which is 35 R_s for a 1.4 $M_\odot$ neutron star. The central parts of the disk are then unobservable. As it is the innermost parts of the disk which rotate most rapidly, and so contribute most to the broadening, this will reduce the measured line width. From the model of Laor (1993), as implemented in the XSPEC spectral fitting package (Shafer et al. 1991), the FWHM of the line reduces to $\sim$0.9 keV for an inner radius of 35 R_s as compared to $\sim$2 keV for 5 R_s.

While the physical width of the line is then consistent with that observed, the line energy and equivalent width are still too low. The observed line energy can be obtained only if the disk surface is ionized. For very highly ionized material, where the predominant iron state is He-like at 6.7 keV, the fluorescent yield also increases by a factor of 2 giving a line of 60 eV equivalent width. However, the 1 σ error on the line allows solutions of much lower ionization state, where the fluorescent yield is close to that for cold material. The observed equivalent width then requires an overabundance of iron of approximately twice solar, as seen in Cyg X-1 (Kitamoto et al. 1984).

This substantial ionization of the disk is hard to achieve by photoionization. At the assumed magnetospheric radius of 150 km, a standard Shakura-Sunyaev disk predicts a density of $\sim 10^{21}$–10^{23} cm^{-3} for a viscosity of $\alpha \sim$ 1–0.01. The ionization parameter of the inner radius of the disk is then $\xi = L/nr^2 = 44$–0.4 (Kallman & McCray 1982) and will decrease outward, so that iron is ionized by photoelectric illumination to only $\sim$Fe XI–XV, insufficient to modify the line energy. If photoionization is indeed the dominant disk ionization mechanism, then the vertical density gradient in the disk must be important, so that the less dense outer layers produce the ionized skin of the disk. However, it is also possible to use simply the ion populations caused by the disk temperature. The innermost observable parts of the disk have a temperature of 1–3 $\times$ 10^7 K (α = 1–0.01) corresponding to Fe XX–XXV, which gives a line with energy $\sim$6.6 keV as required.

However the ion populations are maintained, the line energy requires $\xi \sim 10^3$ (Kallman 1991; Kallman & White 1989), while rotation gives the FWHM of the line as 0.9 keV. The line equivalent width is boosted by a factor of $\sim$2 with respect to that from the cold disk from the increased fluorescent yield (Ross & Fabian 1992), giving a total of 60 eV as observed.

Reflection produces a continuum signature as well as line features (Lightman & White 1988; Guilbert & Rees 1988), providing an independent test of our interpretation of the line features. For a cold disk, reflection is suppressed at low energies through photoelectric absorption, and at high energies through Compton downscattering of the incident radiation, the predominance of forward scattering, and the reduction in

the scattering cross section (Klein-Nishima). This leads to a broad band hump between 10 and 100 keV, with a marked iron edge at 7.1 keV. For ionized material the photoelectric opacity at low energies is greatly reduced so that reflection is marked only by the iron edge (now at energies ≥ 7.1 keV) and a high-energy decrease (Lightman & White 1988; Done et al. 1992). If photoionization determines the ion populations, then the reflection spectrum shape changes (most noticeably in the energy of the iron edge) with changing source luminosity, whereas if collisional ionization dominates the reflection spectrum shape should stay approximately constant. Thus there is the theoretical possibility that the ionization mechanism can be determined. Fitting an edge to the data gives a best fit energy at 8.5 keV. While this edge is not significant, it is suggestive that this energy corresponds to highly ionized material. Assuming that this ionized skin also corotates, there will be an additional blueshift to the edge through Doppler motions in the disk (Matt et al. 1991). The calculation of this spectrum is beyond the scope of this paper and the statistical quality of the BBXRT data; however, future missions such as *Astro-D* should be able to test whether the ionized disk skin is indeed the source of the line emission by fitting such reflection spectra to the continuum emission from Cyg X-2.

REFERENCES

Chiappetti, L., et al. 1990, ApJ, 361, 596
Cowley, A. P., Crampton, D., & Hutchings, J. B. 1979, ApJ, 231, 539 (CCH)
Crampton, D., & Cowley, A. P. 1980, PASP, 92, 147
Done, C., Mulchaey, J. S., Mushotzky, R. F., & Arnaud, K. A. 1992, ApJ, 395, 275
George, I. M., & Fabian, A. C. 1991, MNRAS, 249, 352
Guilbert, P. W., & Rees, M. J. 1988, MNRAS, 233, 475
Hasinger, G., Langmeier, A., Sztajno, M., Trümper, J., Lewin, W. H. G., & White, N. E. 1986, Nature, 319, 469
Hasinger, G., van der Klis, M., Ebisawa, K., Dotani, T., & Mitsuda, K. 1990, A&A, 235, 131
Hirano, T., Hayakawa, S., Kunieda, H., Makino, F., Masai, K., Nagase, F., & Yamashita, K. 1984, PASJ, 36, 769
Hirano, T., Hayakawa, S., Nagase, F., Masai, K., & Mitsuda, K. 1987, PASJ, 39, 619
Kahn, S. M., & Grindlay, J. E. 1984, ApJ, 281, 826
Kallman, T. R. 1991, in Lecture Notes in Physics, 385, Iron Line Diagnostics in X-ray Sources, ed. A. Treves, G. C. Perola, & L. Stella (Berlin: Springer-Verlag), 87
Kallman, T. R., & McCray, R. A. 1982, ApJS, 50, 263
Kallman, T. R., Vrtilek, S. D., & Kahn, S. M. 1989, ApJ, 345, 498
Kallman, T. R., & White, N. E. 1989, ApJ, 341, 955
Kitamoto, S., Miyamoto, S., Tanaka, Y., Ohashi, T., Kondo, Y., Tawara, Y., & Nakagawa, M. 1984, PASJ, 36, 731
Laor, A. 1993, ApJ, 402, 441
Lightman, A. P., & White, T. R. 1988, ApJ, 335, 57
Matt, G., Perola, G. C., & Piro, L. 1991, A&A, 247, 25
Matt, G., Perola, G. C., Piro, L., & Stella, L. 1992, A&A, submitted
McClintock, J. E., Petro, L. D., Hammerschlag-Hensberge, G., Proffitt, C. R., & Remillard, R. A. 1984, ApJ, 282, 794
Mitsuda, K., et al. 1984, PASJ, 36, 741
Mitsuda, K., et al. 1989, PASJ, 41, 97
Podznakov, L. A., Sobol, I. M., & Sunyaev, R. A. 1983, Astrophys. & Space Sci. Rev., 2, 189
Ross, R., & Fabian, A. C. 1992, MNRAS, in press
Schulz, N. S., Hasinger, G., & Trümper, J. 1989, A&A, 225, 48
Serlemitsos, P. J., et al. 1992, in Proc. 28th Yamada Conference of the Frontiers of X-Ray Astronomy (Tokyo: Universal Academy), 221
Shafer, R. A., Harberl, F., Arnaud, K. A., & Tennant, A. F. 1991, ESA publication TM-09
Stella, L. 1988, Mem. Soc. Astron. Italiana, 59, 185
Sunyaev, R. A., & Titarchuk, L. G. 1980, A&A, 86, 121
van der Klis, M. 1989, ARA&A, 27, 517
Vrtilek, S. D., Kahn, S. M., Grindlay, J. E., Helfand, D. J., & Seward, F. D. 1986, ApJ, 307, 698
Vrtilek, S. D., Swank, J. H., Kelley, R. L., & Kahn, S. M. 1988, ApJ, 329, 276
Vrtilek, S. D., McClintock, J. E., Seward, F. D., Kahn, S. M., & Wargelin, B. J. M. 1991, ApJS, 76, 1127
Weaver, K. A., et al. 1992, in preparation
White, N. E., Peacock, A., & Taylor, B. G. 1985, ApJ, 324, 363
White, N. E., Peacock, A., Hasinger, G., Mason, K. O., Manzo, G., Taylor, B. T., & Branduardi-Raymont, G. 1986, MNRAS, 218, 129
White, N. E., Stella, L., & Parmar, A. N. 1988, ApJ, 324, 363